Full–length paper

Extension of HRTEM resolution by semi–blind deconvolution method and Gerchberg–Saxton algorithm: application to grain boundary and interface

Fu-Rong Chen[1,*], Hideki Ichnose[2], Ji-Jung Kai[1] and Li Chang

[1]Department of Engineering and System Science, National Tsing Hua University, Hsinchu, Taiwan, [2]Department of Materials Science and Engineering, Tokyo University, Tokyo, Japan and [3]Department of Materials Science and Engineering, National Chiao Tung University, Hsinchu, Taiwan
*To whom correspondence should be addressed. E-mail: frchen@ess.nthu.edu.tw

Abstract | A generalized maximum entropy method coupled with Gerchberg–Saxton algorithm has been developed to extend the resolution from high-resolution TEM image(s) for weak objects. The Gerchberg–Saxton algorithm restores spatial resolution by operating real space and reciprocal space projections cyclically. In our methodology, a generalized maximum entropy method (Kullback–Leibler cross entropy) dealing with weak objects is used as a real space (P1) projection. After P1 projection, not only are the phases within the input spatial frequencies improved, but also the phases in the next higher frequencies are extrapolated. An example of semi-blind deconvolution (P1 project only) to improve the resolution in SiC twin boundary is shown. The nature of the bonding in this twin boundary is Si-C but it was rotated 180° along the boundary normal. The optimum solution from P1 projection can be further improved by a P2 projection. The square roots of diffraction intensities from a diffraction pattern are then substituted to complete a cycle operation of the Gerchberg–Saxton algorithm. Application examples of Gerchberg–Saxton algorithm to solve the atomic structure of defects (2×1 interfacial reconstruction and dislocation) in $NiSi_2$/ Si interfaces will be shown also.

Introduction

The trend in development of materials technology, including microelectronics, magnetic recording heads and opto-electronics, is the reduction of device size to near nanometre scale. The interface in materials becomes a crucial factor for controlling the properties and performance of the devices at this level. An example of transmission electron microscope (TEM) study in the interfacial structure and reaction in sub-half micron devices is given in reference [1]. In the past, the high-resolution TEM (HRTEM) has provided useful information of atomic structure in a nanometre area of samples. However, the phases in the low spatial frequency region (less than information limit) were modified and the information in the higher spatial frequency region were cut off by the lens contrast

transfer function (CTF), so that direct correlation of the HRTEM image of crystal structure is not trivial. Furthermore, a resolution of 0.2 nm is not enough to determine the interfacial structure quantitatively without ambiguity. For example, dumb-bell distances in the most popular materials, Si, SiC, and GaN, for application in microelectronics and opto-electronics are 0.136, 0.106, and 0.112 nm, respectively, which cannot be revealed directly with a 0.2 nm resolution microscope. The current development of hardware in Cs corrector and mono-chromator may provide a solution in the near future [2,3]. Numerical reconstruction methods in real space, such as focal variation holography [4–8], and tilt-beam holography methods [9] that use a series of HRTEM images, have been proposed to recover the information in the exit surface of the specimen level, which contains the structural information

Fig. 1 (a) A blurred image of a woman. This image is blurred with a point spread function of 10×10 pixels. (b) A deconvoluted image resulting from minimization of eq. (1).

of non-aberration. Unlike real space reconstruction methods, the 'direct method' of electron crystallography that utilizes a HRTEM image and electron diffraction intensities has been applied [10–15] to extend the structural information beyond the Scherzer resolution of a TEM. The direct method is a set of mathematical techniques, e.g. the Sayre equation [16], for extending the phases of diffracted beams to higher spatial frequency, and has given only amplitude information that is equal to the square of the measured intensity [17–20]. In the direct method, the HRTEM image was used to provide the initial phase information in the low spatial frequency region. The electron diffraction intensities in this approach were obtained from sufficiently thin specimen regions to avoid dynamical effects and the results were interpreted within the kinematical approximation.

In our previous publication [21], the Gerchberg–Saxton algorithm [22,23] was used to extend the structural information, which also utilizes HRTEM image(s) and electron diffraction intensities. The HRTEM images contain distorted phase information in low frequency, while the diffraction pattern provides no phase information but the diffraction amplitudes are preserved up to nearly 20 nm^{-1}. The Gerchberg–Saxton algorithm consists of two operations, namely real space (P1) and reciprocal space (P2) projections. These two projections operate cyclically. In the real space projection, a constrained maximum entropy method (MEM) was used to extrapolate the phases to the higher spatial frequency region based on HRTEM images. This process is denoted as P1 projection and is a real space operation. The constrained MEM used in our previous paper is different from that in previous work by Huang *et al*. [13], in which case the maximum entropy is used to determine the optimum value of underfocus. The maximum entropy formula we used is also different from that for X-ray crystallography [24], and that proposed by Sinkler *et*

al. [15] and Marks *et al*. [25,26] for surface crystallography, due to the weak phase object constraint term we coupled with the entropy term in the Lagrangian equation. In this paper, we present an improved version of our previous method [21] based on the Gerchberg–Saxton algorithm [22,23] to extend the resolution of HRTEM images. The improvement of our method is two-fold. (1) A generalized maximum entropy method (Kullback–Leibler cross entropy [27]) to deal with complex signal for weak scattering, in which case the amplitude and the phase part of the exit wave are included in the Lagrangian function. This allows this method to work better in the thicker sample regime than the weak phase version does. (2) The maximum entropy deconvolution method relies on the knowledge of the CTF of the objective lens. Usually, the CTF is determined from a power spectrum of amorphous region in the edge of the sample. We present here a method for determining the CTF from the crystalline experimental image itself. Therefore, we can extrapolate the phase information to higher frequency with the real space operator–maximum entropy deconvolution method simply only from a given experimental HRTEM image, since the information of contrast transfer function CTF (or point spread function) can be implictly extracted from the image itself. This process is called semi-blind deconvolution. An application case of semi-blind deconvolution with Gerchberg–Saxton algorithm to solve the atomic structure for SiC twin boundary and NiSi$_2$/ Si interfaces will be shown. Details of the process in semi-blind deconvolution and Gerchberg–Saxton algorithm will be given in a later section.

Generalized maximum entropy method for weak object

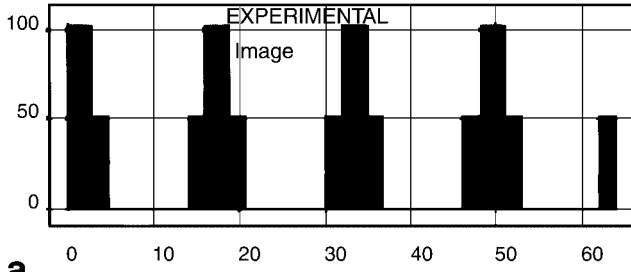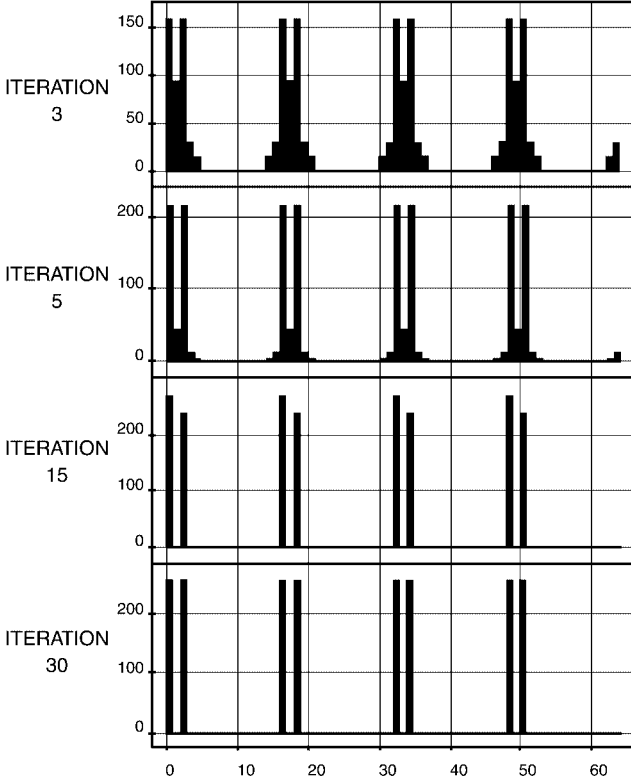The resolution of a blurring image (or signal) I^{exp} can be

Fig. 2 (a) A one-dimensional blurring signal. The blurring function is a 5-pixel flat hat function. (b) The restoration of the signal as the iteration step increases in minimiztion of eq. (1).

improved by minimization of the following Lagrangian function L with providing a known function $B(r)$, which is a point spread function of objective lens.

$$L = -\Sigma_i V(r)\ln(V(r)/D(r)) - \lambda_0(V(r)-f) - \Sigma_j\lambda_1\Sigma_i(V(r)*B(r) - I_j^{exp} - e_j) - \Sigma_j\mu_j\{(e_j/\sigma_j)^2 - \chi^2\} \tag{1}$$

Where $V(r)$ is an optimum solution we wish to find and r is a position vector in the image space. The summation operates on the pixel with index i. $V(r)$ contains phase information of higher spatial frequency domain than that in I^{exp}. The first term in the Lagrangian function is the cross entropy, while the rest of three terms are the constraints for the optimum solution. The $D(r)$ in the entropy term is a default guess, which can

be obtained using a Wiener filter [28]. The λ_o, λ_1 and μ_j are three Lagrangian multipliers for three constraints. The first constraint sets the constant flux in the optimum solution $V(r)$, and the second constraint sets the condition that the optimum $V(r)$ convolutes with $B(r)$ to be as close to the I^{exp} as possible. The e_j and σ_j are the noise and variance in the jth experimental defocused image, respectively. The last constraint sets the limitation for the target χ^2. This maximum entropy deconvolution method has been extensively used in the area of astronomy for image deconvolution to improve the resolution of images [29,30]. An example of maximum entropy deconvolution is given in Fig. 1. Figure 1a is a blurring image of a woman, which is I^{exp} in eq. (1). This image is blurred with a point spread function $B(r)$ of 10×10 pixels. The $D(r)$ is initially set to be identical to I^{exp}. The final optimum solution $V(r)$ (or MEM solution) after 1000 iterations in minimization of eq. (1) is given in Fig. 1b. We can see that the fine detail in the image has been restored. In the Fourier space, the phases in the higher frequency region have been extrapolated back correctly. Another example is given in Fig. 2. A one-dimensional blurring signal is shown in Fig. 2a. The blurring function is a 5-pixel flat hat function. Figure 2b shows the restoration of the signal as the iteration step of minimization of eq. (1) increases.

In the weak phase object case, the second constraint in eq. (1) is replaced with $1 + 2*\sigma V(r)*F^{-1}(\text{imag}(T(H))) - I_j^{exp} - e_j$, where σ is an interaction constant and $V(r)$ is the projected potential as well as the phase of the exit wave, * means convolution operation. H is a reciprocal lattice vector and $F^{-1}(\text{imag}(T(H)))$ is an inverse Fourier transform of imaginary part of $T(H)$, the lens CTF, including coherency of imaging system for weak phase object, and is equivalent to $B(r)$ in eq. (1). $T(H)$ is given below

$$T(H) = \exp(i\chi_1(H))\exp(-\chi_2(H)) \tag{2}$$

$$\chi_1(H) = \pi\lambda\Delta f H^2 + \tfrac{1}{2}\pi C_s\lambda^3 H^4$$

$$\chi_2(H) = \tfrac{1}{2}\pi^2\lambda^2\delta f H^4 + \pi^2(\alpha^2/\lambda^2)q$$

C_s is the spherical aberration coefficient; λ is the wavelength; δf is the focal spread of objective lens; and α is the convergence angle of electron beam.

$$q = (\lambda\Delta f H + C_s\lambda^3 H^3)^2$$

The detailed explanation of the algorithm in weak phase approximation can be found in our previous paper [21]. To extend the applicability of the maximum entropy deconvolution method to the thicker sample, the weak object approximation is considered within the Lagrangian function. In the weak object case, a small variation in amplitude $\mu(r)$ and phase $V(r)$ of exit wave Ψ_e are allowed. The exit wave Ψ_e and intensity distribution I in the image plane can be written as follows [31]:

Initial V(r) and μ(r)

Compute optimum V(r) and ,
equation (6) and (7)

a) Compute I^{pred} from equation (4)
b) Compute $I^{\text{pred}} - I^{\text{exp}}$

Compute λ_{1j} and μ_j

from minimization of potential function Z,
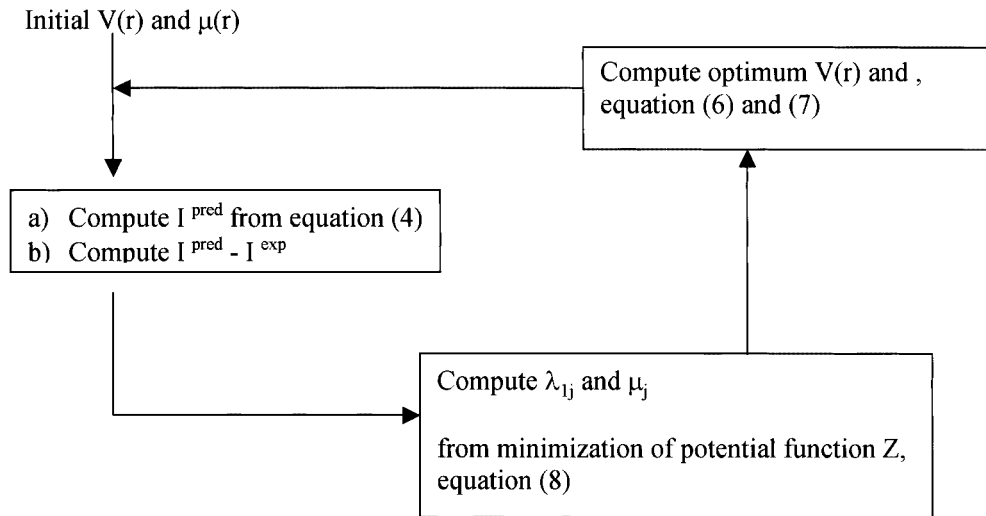equation (8)

Fig. 3 A flow chart of the minimization process of constrained maximum entropy method.

$$\Psi_e = 1 + \mu(r) + i\sigma V(r), \text{ where } \mu(r) \sim 1 - V(r)^2/2 \quad (3)$$

$$I = 1 + 2\mu(r)*\text{F}^{-1}(\text{real}(T(H))) + 2\sigma V(r)*\text{F}^{-1}(\text{imag}(T(H))) \quad (4)$$

The Kullback–Leibler cross entropy is defined to improve the resolution for the complex image (complex signal) problem using maximum entropy method [27]. The entropy term in eq. (1) is modified to be

$$-\Sigma_i\mu(r)\ln(\mu(r)/D_\mu(r)) - \Sigma_i V(r)\ln(V(r)/D_v(r))$$

where $D_\mu(r)$ and $D_v(r)$ are the initial guesses. $D_v(r)$ is roughly close to the default image obtained from a Wiener filter, as in the weak phase object approximation. Although $\mu(r)$ and $V(r)$ are independent variables, $D_\mu(r)$ is set to be $1 - D_v(r)^2/2$ in the beginning. The Lagrangian function in eq. (1) is therefore modified to be

$$
\begin{aligned}
L = &-\Sigma_i\mu(r)\ln(\mu(r)/D_\mu(r)) - \Sigma_i V(r)\ln(V(r)/D_v(r)) \\
&- \lambda_{o\mu}(\mu(r) - f_\mu) - \lambda_{ov}(V(r) - f_v) - \Sigma_j\lambda_{1j}\Sigma_i(1 + 2\mu(r)*\text{F}^{-1} \\
&(\text{real}(T(H))) + 2\sigma V(r)*\text{F}^{-1}(\text{imag}(T(H))) - I_j^{\text{exp}} - e_j) \\
&- \Sigma_j\mu_j\{(e_j/\sigma_j)^2 - \chi^2\} \quad (5)
\end{aligned}
$$

The constraints in the constant flux now are set for both $\mu(r)$ and $V(r)$, and the second constraint is modified to be

$$1 + 2\mu(r)*\text{F}^{-1}(\text{real}(T(H))) + 2\sigma V(r)*\text{F}^{-1}(\text{imag}(T(H))) - I_j^{\text{exp}} - e_j$$

Following the same procedure given in the previous paper, the optimum solution of $\mu(r)$ and $V(r)$ can be found by setting partial derivation of L with respect to $\mu(r)$, $V(r)$ and e_j zero, $\partial L/\partial\mu(r) = 0$, $\partial L/\partial V(r) = 0$ and $\partial L/\partial e_j = 0$,

$$
\begin{aligned}
\mu(r) = &f_\mu D_\mu(r)\exp(-2\Sigma_j\lambda_{1j}*\text{F}^{-1}(\text{real}(T(H)))) / \\
&\Sigma_i D_\mu(r)\exp(-2\Sigma_j\lambda_{1j}*\text{F}^{-1}(\text{real}(T(H)))) \quad (6)
\end{aligned}
$$

$$
\begin{aligned}
V(r) = &f_v D_v(r)\exp(-2\sigma\Sigma_j\lambda_{1j}*\text{F}^{-1}(\text{imag}(T(H)))) / \\
&\Sigma_i D_v(r)\exp(-2\sigma\Sigma_j\lambda_{1j}*\text{F}^{-1}(\text{imag}(T(H)))) \quad (7)
\end{aligned}
$$

λ_{1j} and μ_j in last two equations can be found from derivation of a potential function Z with respect to λ_{1j} and μ_j, $\partial Z/\partial\lambda_{1j} = 0$ and $\partial Z/\partial\mu_j = 0$, where

$$
\begin{aligned}
Z = &\Sigma_j\lambda_{1j} - \log\{\Sigma_i\exp(-2\Sigma j\lambda_{1j}*\text{F}^{-1}(\text{real}(T(H))))\} \\
&- \log\{\Sigma_i\exp(-2\sigma\Sigma_j\lambda_{1j}*\text{F}^{-1}(\text{imag}(T(H))))\} \\
&- (\frac{1}{4}\mu_j)\lambda^2_{1j}\sigma_j^2 - I_j^{\text{exp}} - \mu_j\chi^2 \quad (8)
\end{aligned}
$$

A flow chart of minimization iteration process is given in Fig. 3. When $V(r) \ll 1$, $\mu(r)$ is much less than $V(r)$. The maximum entropy algorithm for the weak scattering object case degenerates to that in the weak phase case. The program is written in the script language in Gatan Digital Micrograph.

Semi-blind deconvolution

For minimization of the Lagrangian function in usual deconvolution process, we need to know the point spread function (or CTF) of the objective lens and an experimental image. In the case of a high-resolution image, the lens CTF usually can be determined from a power spectrum from amorphous region in the edge of sample [32]. However, quite often, amorphous materials in the edge of sample may be not available or far from where the HRTEM image is recorded. In such cases CTF cannot be determined well. Deconvolution without sufficient or even no information of CTF (or point spread function) is called blind deconvolution [33,34]. In some special case, the point spread function can be identified from the cepstrum of experimental image I_j^{exp} [33,34] such that the deconvolution process can be carried out only with given experimental image(s). The cepstrum is defined as Fourier integral transform of $\log(\text{F}(I_j^{\text{exp}}))$ [33]. We called this deconvolution process semi-blind deconvolution, where the information of CTF can
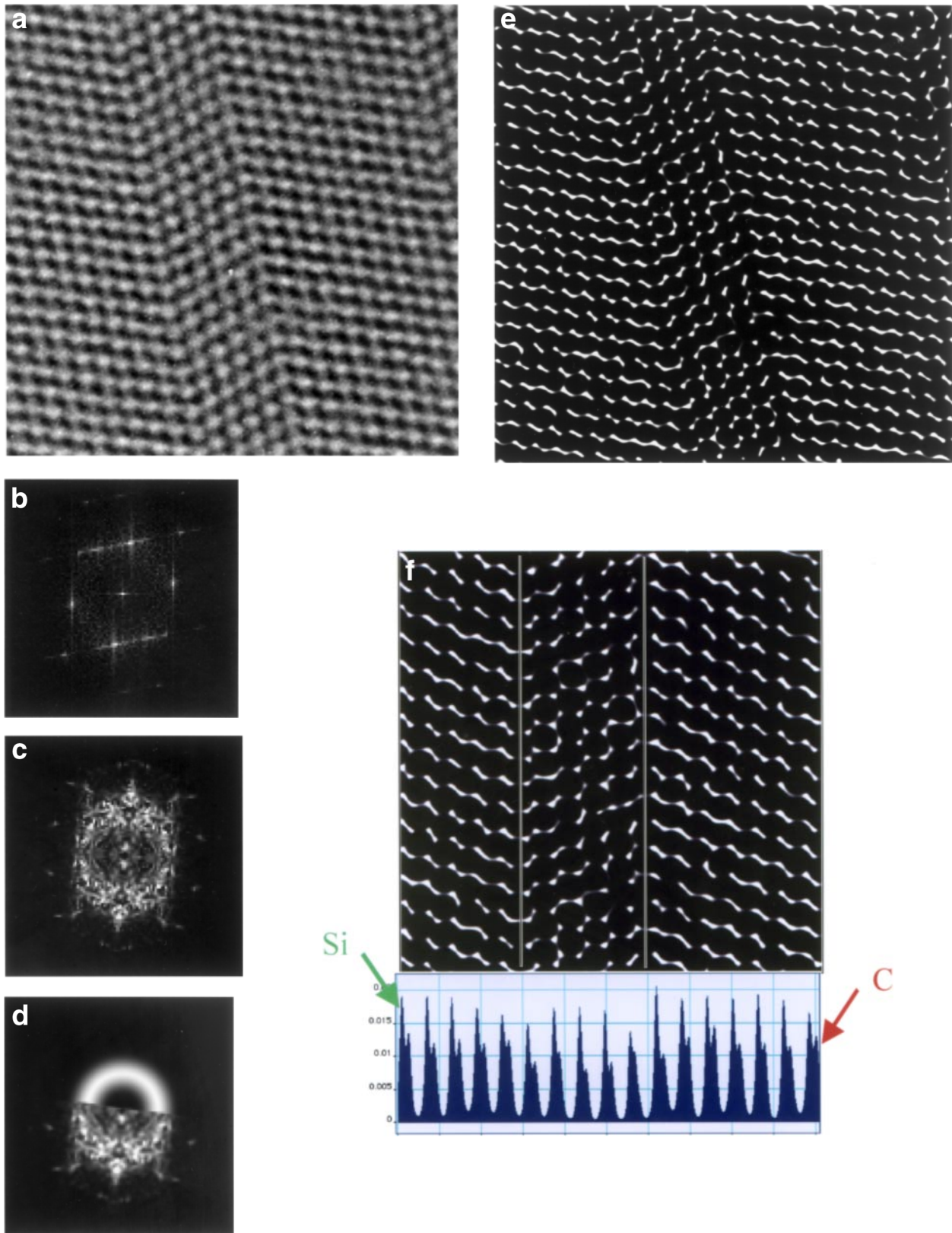
Fig. 4 (a) HRTEM image of SiC twin boundaries recorded using ultra-high voltage TEM [36]. (b) Power spectrum of (a). (c) Power spectrum after stripping the peaks contributing from crystal periodicity. (d) A simulated $|\sin(\chi_1(H))\exp(-\chi_2(H))|^2$ pasted with (c). The parameters of the simulated CTF are voltage = 1250 kV, C_s = 1.4 mm, C_c = 2.5 mm, divergent angle α =1 mrad, Δf = –42.4 nm, and magnitude and direction of the astigmatism, A = 1 nm and ϕ_a = 82.5°. (e) The phase part of optimum solution $V(r)$. (f) Profile of integrated intensity parallel to the twin boundary.
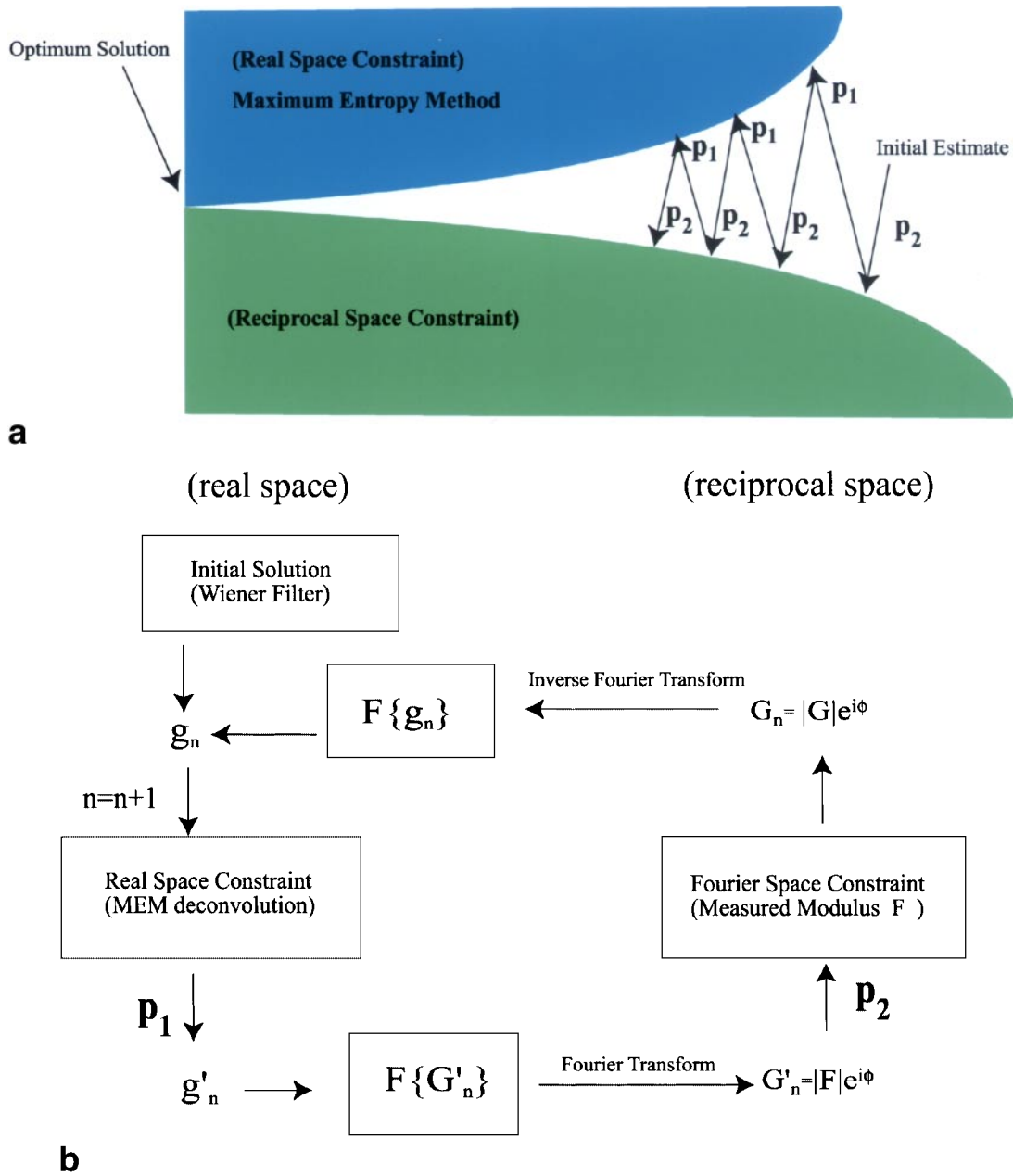
Fig. 5 (a) A graphic presentation of the Gerchberg–Saxton algorithm. (b) A flow chart version of Gerchberg–Saxton algorithm and the cyclic procedures of P1 and P2 operations.

be extracted from the experimental image itself. Estimation of the CTF from HRTEM crystal image using cepstrum or power spectrum usually is not applicable, since the peaks associated with crystal periodicities dominate in the power spectrum or cepstrum. Here, we present a method to estimate the CTF from the HRTEM crystal image(s), which is recorded from a slightly surface-contaminated sample. The idea is based on a speckle technique to improve the signal-to-noise ratio in the reciprocal space [35]. We demonstrate this idea here with a working example. Figure 4a shows a HRTEM image of SiC twin boundaries recorded using ultra-high voltage TEM [36]. The image size is 1024×1024 pixels. The dumb-bell distance

in SiC is near 0.106 nm, which was not directly revealed from this HRTEM image. A power spectrum of Fig. 4a is shown in Fig. 4b, and shows clear signal of the peaks associated with the periodicities of the twin in SiC. There is weak information about the CTF in the background of power spectrum, which is contributed from the surface contanmination. This weak information in the background can be further reduced by averaging of many power spectra from a sub-area (256×256 pixels) of the experimental image. The averaging power spectrum can be expressed as $\Sigma |F(I_k^{exp})|^2 / N$. I_k^{exp} is a sub-image from the whole image denoted as I^{exp}, N is the total number of the sub-image, and k is a dummy index of the sub-image. F is

a Fourier transformation operator and Σ is the summation operation. The power spectrum of the whole image is expressed as $|F(I^{exp})|^2$. Intensities of peaks in the average power spectrum are normalized with respect to those in the power spectrum of the whole image $|F(I^{exp})|^2$. The peaks associated with the crystal periodicities can then be removed by subtracting the $|F(I^{exp})|^2$ from the normalized average $\Sigma|F(I_k^{exp})|^2/N$. The resultant power spectrum is shown in Fig. 4c. The power spectrum from the surface contamination can then be enhanced and the CTF is revealed. If we provide the data of accelerating voltage of TEM (1250 kV), C_s (1.4 mm), C_c (2.5 mm), and divergent angle α (1 mrad), the underfocus and astigamatism can be estimated by fitting the maximum intensity of Fig. 4c with the $|\sin(\chi_1(H))\exp(-\chi_2(H))|^2$ in eq. (2). The underfocus Δf in eq. (2) is replaced with an effective underfocus Δf^{eff}, if the astigmatism is included in the lens aberration function [37]. $\Delta f^{eff} = \Delta f + A\cos2(\phi - \phi_a)$, where A and ϕ_a are the magnitude and direction of the astigmatism, respectively. The development of the quantitatively fitted algorithm is in progress, but the qualitatively estimated data for underfocus value and astigmatism are $\Delta f = -42.4$ nm, $A = 1$ nm and $\phi_a = 82.5°$. Figure 4d shows a simulated $|\sin(\chi_1(H))\exp(-\chi_2(H))|^2$ that is pasted with Fig. 4c for comparison. The experimental image in Fig. 4a can then be deconvoluted either using a weak phase object or weak object approximation. The phase part $V(r)$ is shown in Fig. 4e. Although the dumb-bell structure in SiC can be revealed after 1500 iterations in the maximum entropy deconvolution process, the bonding nature of either Si-Si, C-C or Si-C bond across the twin boundary still cannot be revealed directly from the deconvoluted solution $V(r)$. The profile of integrated intensity parallel to the twin boundary is obtained and shows modulation of stong and weak peaks (Fig. 4f). The stronger peaks correspond to Si and the weaker peaks correspond to C, suggesting that the bonding nature of Si-C does not change across the twin boundary, but that it was rotated 180° along the normal of twin boundary.

Gerchberg–Saxton algorithm and results

Although the resolution of the HRTEM can be improved from the constrained MEM deconvolution process alone (the real space P1 projection), as we can see from the example of SiC twin boundary given in the previous section, Gerchberg–Saxton algorithm suggested that the information could be refined and further improved by cyclically operating real space (P1) and reciprocal space (P2) projections. This is the central idea of the Gerchberg–Saxton algorithm, which recovers the information from partially known phase and magnitude [23]. A graphic presentation of the Gerchberg–Saxton algorithm is given in Fig. 5a. In the P1 projection, a constrained MEM is used not only to modify the phase in the input frequency domain but also to extrapolate the phases to higher spatial frequency region based on the HRTEM images. In the P2 projection, the square root of the integrated intensities from
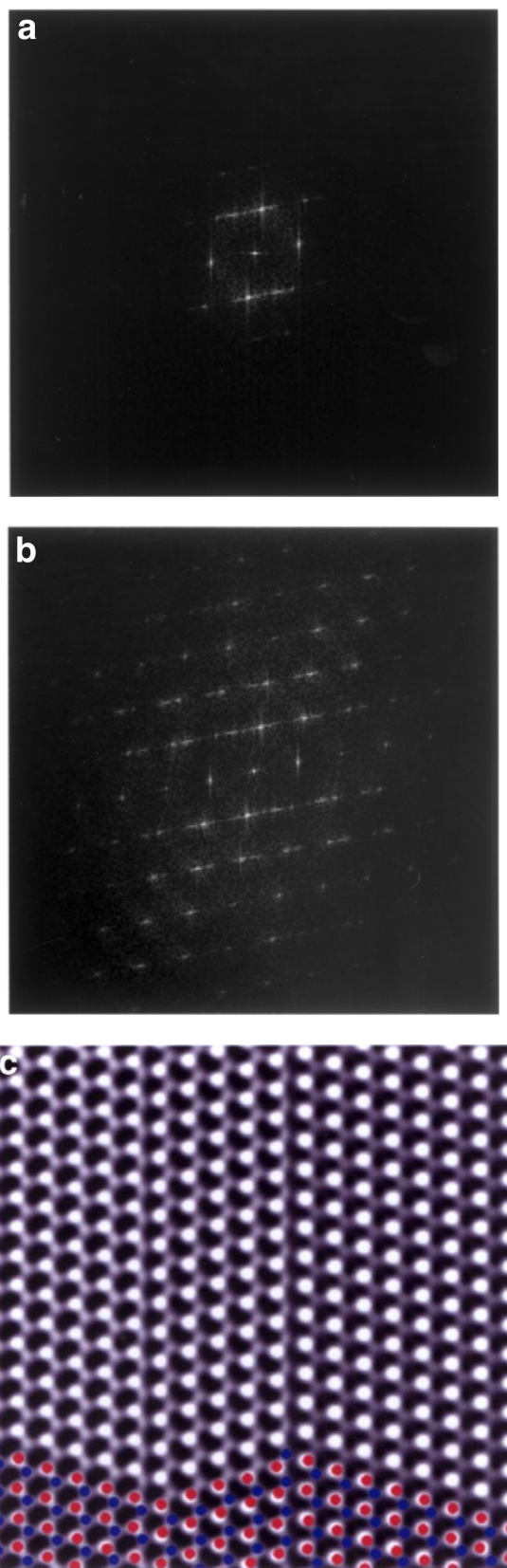

Fig. 6 (a) and (b) The power spectra of Figs 4a and 4e, respectively. (c) The optimum solution of $V(r)$ after 1000 iterations in Gerchberg–Saxton cyclic operations. The red circles represent Si atoms and the blue circles represent C atoms.
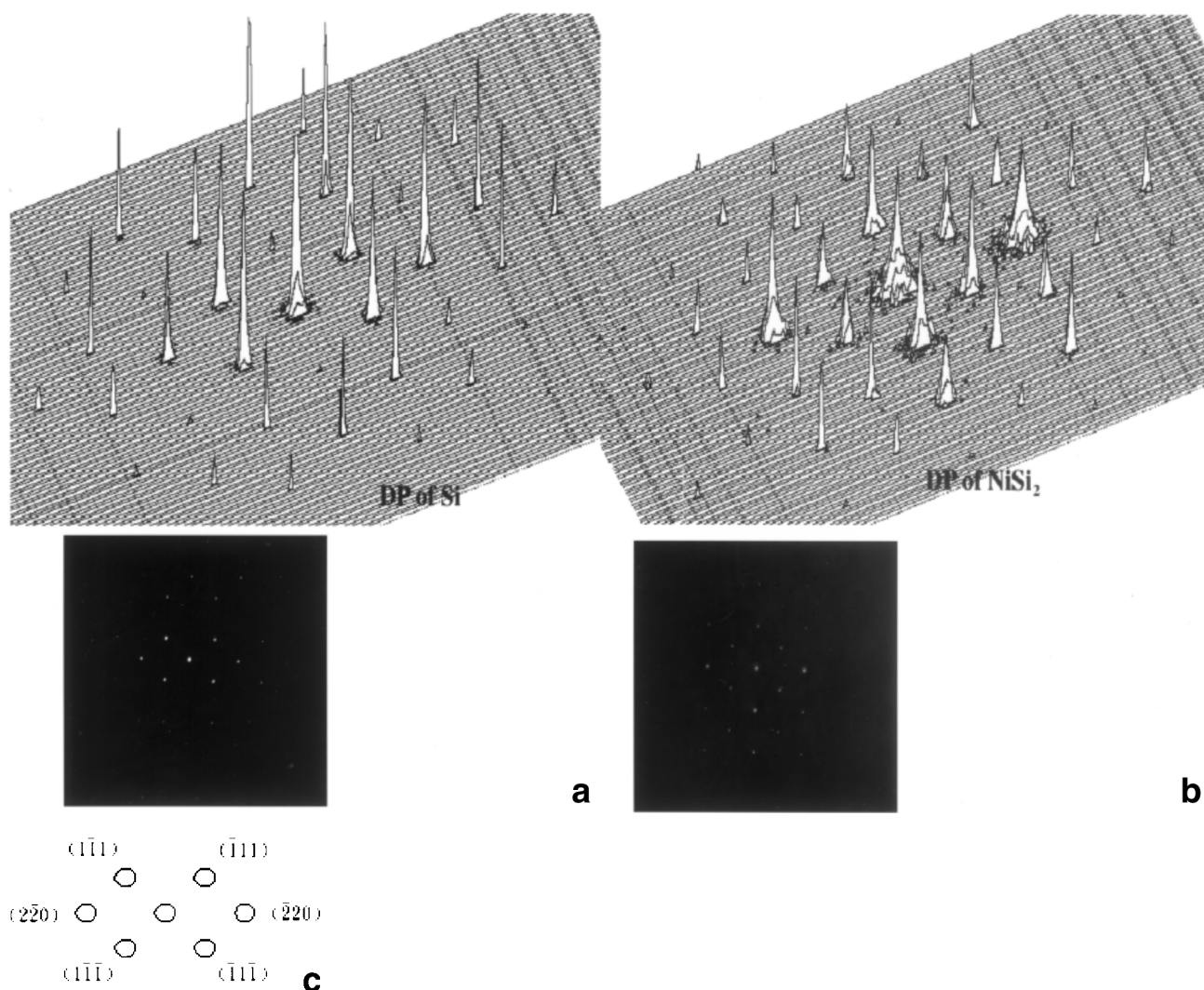
Fig. 7 (a) and (b) Diffraction patterns and intensities of Si and $NiSi_2$, respectively. (c) Indexed schematic pattern for (a) and (b).

the diffraction pattern is substituted but the phases are saved. To review the dumb-bell for SiC, $NiSi_2$, and Si, we only used diffraction amplitude up to {004} diffractions. We cyclically operated the P1 and P2 projections until the satisfatory solution was found in both real and reciprocal spaces. The detailed processes of these two projections are given in Fig. 5b, which shows a flow chart version of the Gerchberg–Saxton algorithm and the cyclic procedures of P1 and P2 operations. The g_n is an initial default in real space. In the beginning it was obtained using a Wiener filter. The g'_n is a MEM solution after P1 projection, i.e. a deconvoluted solution from MEM. It contains phase information of higher spatial frequencies. G'_n is a Fourier transform of g'_n. P2 operation is a process of replacing the modulus $|G'_n|$ by the measured diffraction amplitude $|G_n|$. The phase information is saved in P2 projection. After P2 operation, G'_n becomes G_n. The inverse Fourier transformation brings G_n back to real space and the new solution is called g_{n+1}. The g_{n+1} is set to be a new default solution that contains higher spatial information than g_n. The application example of

Gerchberg–Saxton algorithm in SiC twin boundary is given here. Figures 6a and 6b show the power spectra of Figs 4a and 4e, respectively. The phase information is extrapolated to the higher frequency domain in Fig. 6b, which is equivalent to higher resolution, and is achieved in real space in Fig. 4e. Figure 6c shows the resultant solution of $V(r)$ after 1000 iterations of P1 and P2 cyclic operations. The Si and C are more distinguishable than that in Fig. 4e.

This algorithm is applied to solve the atomic structure of defects in epitaxial $NiSi_2$ / Si interface, which is usually called type A interface. The type A $NiSi_2$ / Si interface usually has processes of structural multiplicity [38]. $NiSi_2$ has a face-centre cubic unit cell with CaF_2 structure and lattice constant $a = 0.5406$ nm. Si has a diamond cubic structure with lattice constant $a = 0.543$ nm. They have 0.4 % of lattice misfit. The diffraction patterns of $NiSi_2$ / Si are recorded in Fuji imaging plate near the interface with smallest electron beam in a JEOL 4000EX TEM, $C_s = 1.0$ mm, focal spread $\delta f = 15$ nm, and the beam divergence $\alpha = 0.8$ mrad. All HRTEM images
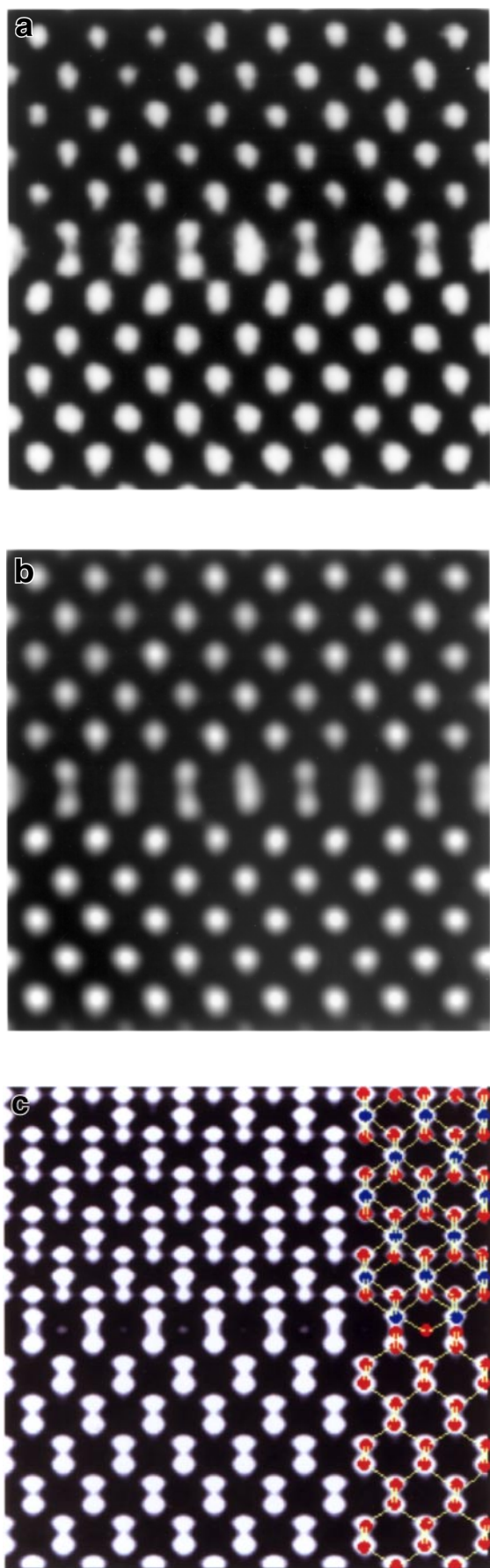
are recorded at an underfocus value near –32 nm, estimated from the thin amorphous region with reference of minimum contrast. A set of diffraction pattern is shown in Figs 7a and 7b. An indexed schematic pattern for (a) and (b) is given in Fig. 7c. In Si, the {002} and {222} diffractions are very weak compared with that in NiSi$_2$. This might imply that there is not too much dynamical effect involved. Figure 8a is an experimental HRTEM image showing a 2 × 1 alternating contrast in the interface. Resolution is extended using the maximum entropy deconvolution method and Gerchberg–Saxton algorithm described above. Figure 8b shows a predicted image calculated using eq. (4) with the optimum solution of $\mu(r)$ and $V(r)$. The simulated image shows very good matches in the image character with the experimental image. The phase part $V(r)$ and a schematic structure pasted with the $V(r)$ is shown in Fig. 8c. We can see that there are alternative Si rich atomic columns in the interface which exhibit a 2 × 1 compositional reconstruction. This type of structure is also observed in the CoSi$_2$ / Si interface [39]. Another example is shown in Fig. 9. Figure 9a shows an interfacial dislocation of ¼<111> type in the NiSi$_2$ / Si interface. This dislocation separates two interfacial domains that have different atomic structure. A predicted image is given in Fig. 9b for comparison with the experimental image. It can be seen that the simulated image calculated using optimum solution has reasonably good matches with the experimental image. The bending of (220) lattice plane associated with strain field of the edge component of this interfacial dislocation near the interface can be seen in the phase part $V(r)$ given in Fig. 9c. A schematic structure deduced from the positions of the bright dots in Fig. 9c is given in Fig. 9d. From Fig. 9d, the extra half-plane associated with this interfacial dislcoation is clearly revealed. We can see that the maximum entropy deconvolution method refines the atomic peak position according to the experimental image, although the diffraction intensities are recorded from a region larger than the image, which gives an average structure in the beginning. A quantitative comparison of the atomic peak positions in Fig. 9c with computational positions from strain field of an interfacial dislcoation will be interesting to study. From this we should be able to make some comments about the precision of this method in determination of the atomic structure [40].

What could be wrong

We have shown that the resolution form HRTEM image(s) can be extended using maximum entropy deconvolution method and diffraction intensities. There are some factors that might cause difficulties in the application of this technique. In the

Fig. 8 (a) Experimental HRTEM image showing a 2 × 1 alternating contrast in the interface. (b) A predicted image calculated using eq. (4) with the optimum solution of $\mu(r)$ and $V(r)$. (c) The optimum phase part $V(r)$ and a schematic structure. Red circles represent Si atoms and blue circles represent Ni atoms.
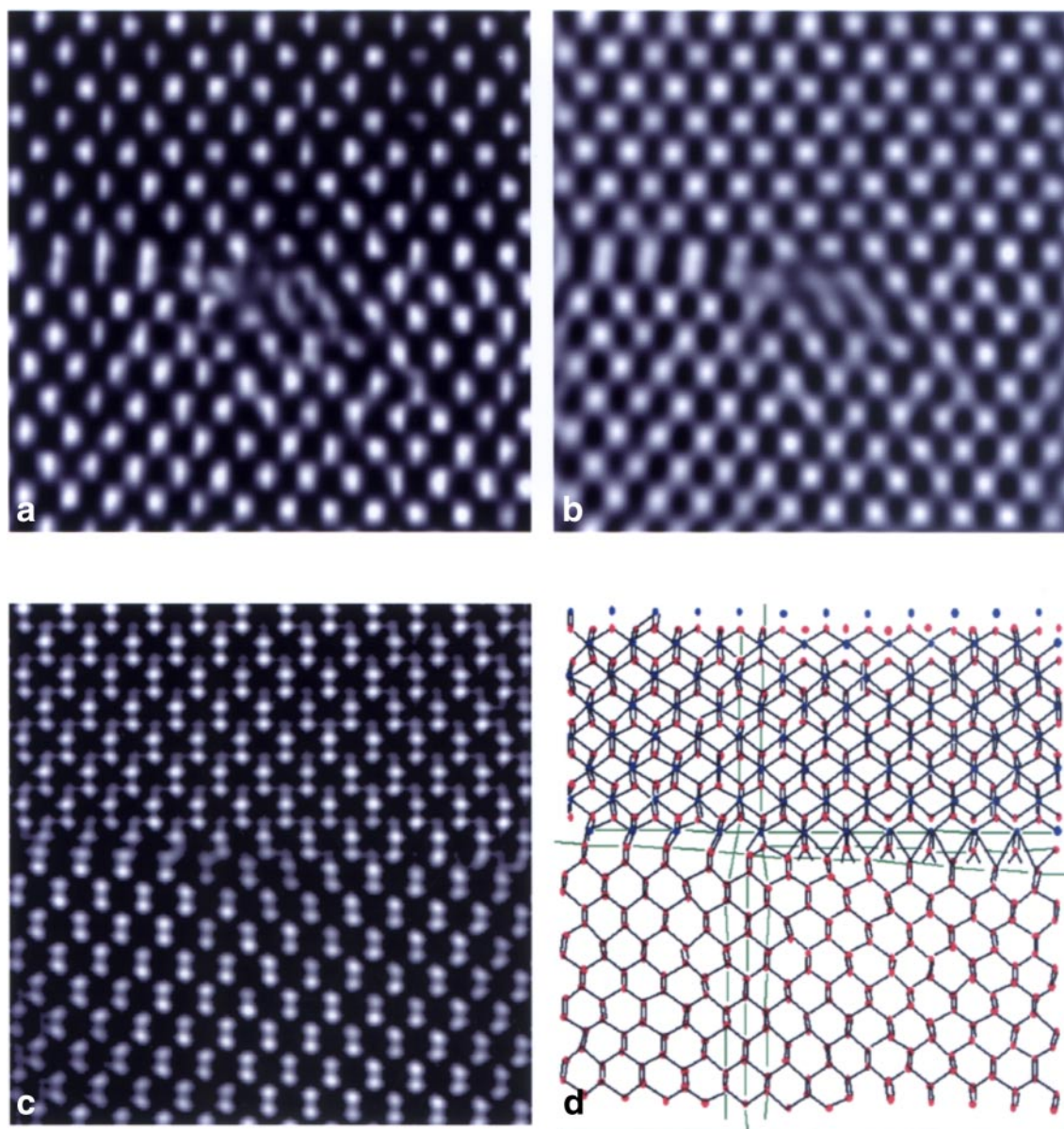
Fig. 9 (a) HRTEM image of an interfacial dislocation of $\frac{1}{4}$<111> type in the $NiSi_2$/ Si interface. (b) A predicted image from optimum solution. (c) The optimum solution of phase part $V(r)$. The bending of {220} lattice plance associated with strain field of the edge component of this interfacial dislocation near the interface can be seen. (d) A schematic structure deduced from the positions of the bright dots. The extra half-plane associated with this interfacial dislocation is clearly revealed. Red circles represent Si atoms and blue circles represent Ni atoms.

real space projection, an initial default solution might be important, since it provides a set of phases in the low frequency domain. If there are errors in the phases in the low frequency domain, the algorithm may take long iteration processes to correct them. In the worst case, the error of phases in an initial default in the low frequency domain might be accumulated to give a wrong solution when the phases are extrapolated to the higher frequency domain. Since the initial default solution is obtained using a Wiener filter [28] with an input CTF, the accuracy needed in the CTF may depend on how far the resolution is extended. In the reciprocal space, even with special care in alignment of the crystal axis, the

same set of diffraction spots may still have roughly 10–15% difference. This arises because the sensitivity of human eyes is not as good as that of imaging plates. The measured intensities from the same set of diffraction spots are averaged if the bulk structure is known and is centro-symmetrical.

The intensities of the atomic peaks in SiC and in $NiSi_2$/ Si do not have any particular relationship with the atomic number of atoms. This method, which is the same as the electron crystallography methods [10–20] utilizing diffraction intensities, only revealed the atomic peak position, but not the exact form of the exit wave. This may be due to the fact that dynamical diffraction becomes more important in high-order diffraction

[15], which causes the linear imaging constraint in our method at high spatial frequencies to break down. The inaccuracy in the deault image may be responsible for this also. A more precise initial default containing higher frequencies may be obtained using more defocus images with well-determined CTF functions. Combination of the focal series [4,7,8] or tilt beam [37] series with our method may make it possible to extend the resolution beyond the information limit numerically.

Concluding remarks

A generalized maximum entropy method coupled with Gerchberg–Saxton algorithm has been developed to extend the resolution of high-resolution TEM images for weak objects. In our methodology, a generalized maximum entropy method (Kullback–Leibler cross entropy) dealing with complex signal in a weak object is used as a real space (P1) projection. A case of semi-blind deconvolution (P1 projection alone) to improve the resolution in SiC twin boundary is shown. The nature of the bonding in this twin boundary is Si-C but it was rotated 180° along the boundary normal. The resolution extension is completed by cyclic operation of P1 (real space) and P2 (reciprocal space) projections. Application examples of resolution extension for 2×1 interfacial reconstruction and interfacial dislocation in $NiSi_2$ / Si have been shown. The bending of {220} plane associated with the strain field of the edge component of an interfacial dislocation can be seen. This implies that the maximum entropy deconvolution method will refine the atomic peak position according to the experimental image, even though the diffraction data come from a larger area. For future work, a quantitative comparison of the atomic peak positions with computational positions is of interest and will allow us to make some comments about the precision of this method in the determination of atomic structure.

References

1   Chang H, Chang L, Chen F-R, Kai J J, Tzou E, Fu J, Xu Z, Egermeimer J, and Chen F-S (1998) High resolution and energy filtering TEM study of interfacial structure and reaction in advanced materials processing. *Acta Mater.* **46**: 2431–2439.

2   Haider M, Rose H, Uhlemann S, Schwan E, Kabius B, and Urban K (1998) A spherical-aberration-corrected 200 kV transmission electron microscope. *Ultramicroscopy* **23**: 768–769.

3   Rose H (1999) Prospects for realizing a sub-A sub-ev resolution EFTEM. *Ultramicroscopy* **78**: 13–25.

4   Van Dyck D, Lichte H, and Van Der Mast K D (1996) Sub-Angstrom structure characterization: the Brite–Euram route towards one Angstrom. *Ultramicroscopy* **64**: 1–15.

5   Kirkland E J (1982) Non-linear high resolution image processing of conventional transmission electron micrographs. *Ultramicroscopy* **9**: 45–64.

6   Thust A, Lentzen M, and Urban (1994) Non-linear reconstruction of the exit plane wave function from periodic high resolution electron microscopy images. *Ultramicroscopy* **64**: 211–230.

7   Coene W, Janssen A J E M, Op de Beeck M, and Van Dyck D (1995) Improving HRTEM performance by digital processing of focal image

seies: results from the CM20 FEG-super TWIN. *Philips Electron Optics Bulletin* **132**: 15–28.

8   Thust A, Coene W M J, Op de Beeck M, and Van Dyck D (1994) Focal-series reconstruction in HRTEM: simulation studies on non-periodic objects. *Ultramicroscopy* **64**: 211–230.

9   Kirkland A I, Saxton W O, Chau K-L, Tsuno K, and Kawasaki M (1995) Super-resolution by aperature synthesis: tilt series reconstruction in CTEM. *Ultramicroscopy* **57**: 355–374.

10   Ishizuka K, Miyazaka M, and Uyeda N (1982) Improvement of electron microscope images by the direct phasing method. *Acta Cryst.* **A38**: 408–413.

11   Fan H-F, Zhong Z Y, Zheng C-D, and Li F-H (1985) Image processing in high resolution electron microscopy using the direct method, I. Phase extension. *Acta Cryst.* **A41**: 163–165.

12   Hu J J, Li F H, and Fan H F (1992) Crystal structure determination of K_2O-bullet Nb_2O_5 by combining high resolution electron microscopy and electron diffraction. *Ultramicroscopy* **41**: 287–397.

13   Huang D X, He W Z, and Li F H (1996) Multiple solution in maximum entropy deconvolution of high resolution electron microscope images. *Ultramicroscopy* **62**: 141.

14   Dong W, Braid T, Fryer J R, Gilmore C J, MacNicol D D, Bricogne G, Smith D J, O'Keefe M A, and Hovmoller S (1992) Electron microscopy at 1 Angstrom resolution by entropy maximization and likehood ranking. *Nature* **355**: 605–609.

15   Sinkler W, Bengu E, and Marks L D (1998) Application of direct methods to dynamical electron diffraction data for solving bulk crystal structures. *Acta Cryst.* **A54**: 591–605.

16   Sayre D (1980) Phase extension and refinement using convolutional and related equation system. In: *Theory and Practice of Direct Methods in Crystallography*, eds Ladd M F C and Palmer R A, pp. 271–286, (Plenum Press, New York).

17   Hoppe W and Gassmann J (1968) Phase correction, a new method to solve partially known structures. *Acta Cryst.* **B24**: 97–108.

18   Gassmann J and Zechmeister K (1972) Limits of phase expansion in direct methods. *Acta Cryst.* **A28**: 270–280.

19   Dorset D, Jap B K, Ho M H, and Glaeser R M (1979) Direct phasing of electron diffraction data from organic crystals: effect of n-beam dynamical scattering. *Acta Cryst.* **A35**: 1001–1009.

20   Debaerdemeker K, Tate C, and Woolfson M M (1985) On the application of phase relationship to complex structures, XXIV. The Sayre tangent formula. *Acta Cryst.* **A41**: 286–290.

21   Chen F-R, Kai J J, Chang L, Wang J Y, and Chen W J (1999) Improvement of resolution by maximum entropy linear image restoration for $NiSi_2$/Si interface. *J. Electron Microsc.* **48**: 827–836.

22   Levi A and Strak H (1987) Restoration from phase and magnitude by generatized projections. In: *Image Recovery: Theory and Application*, ed. Stark H, pp. 277–320, (Academic Press, London).

23   Gerchberg R W and Saxton W O (1972) A practical algorithm for the determination of phase from image and diffraction pictures. *Optik* **35**: 237–246.

24   Bricogne G (1984) Maximum entropy and the fundations of direct methods. *Acta Cryst.* **A40**: 410–445.

25   Marks L D and Landree E A (1998) Maximum-entropy algorithm for surface phasing problem. *Acta Cryst.* **A54**: 296–305.

26   Marks L D, Bengu E, Collazo-Davlia C, Grozea D, Landree E, Leslie C, and Sinkler W (1998) Direct methods for surfaces. *Surface Rev. Lett.* **5**: 1087–1106.

27   Frieden B R and Bajkova A (1994) Bayesian cross-entropy reconstruction of complex images. *Applied Optics* **33**: 219–226.

28   Gonzalez R C and Woods R E (1993) *Digit Image Processing*, pp. 253–304. (Addison-Wesley, Reading, MA.)

29   Wilczek R and Drapatz A(1985) A high accuracy algorithm for maximum entropy image restoration in the case of small data sets. *Astron. Astrophys.* **142**: 9–12.

30   Cornwell T J and Evans K F (1985) A simple maximum entropy deconvolution algorithm. *Astron. Astrophys.* **143**: 77–85.

31 Saxton W O (1978) Computer techniques for image processing in electron microscopy. In: *Advances in Electrons and Electron Physics*, Supplement 10, p. 10, (Academic Press, Inc., New York).

32 Krivanek O L (1976) A method for determining the coefficient of spherical aberration from a single electron micrograph. *Optik* **45**: 97.

33 Cannon M (1976) Blind deconvolution of spatially invariant image blurs with phase. *IEE Trans. Acoustics Speech and Signal Processing* **ASSP 24**: 58–63.

34 Sondhi M M (1972) Image restoration: the removal of spatially invariant degradations. *Proc. IEEE* (*Special Issue on Digital Picture Processing*) **60**: 842–853.

35 Dainty J C and Fienup J R (1987) Restoration from phase and magnitude by generalized projections. In: *Image Recovery*: *Theory and Application*, ed. Stark H, pp. 231–275, (Academic Press, London).

36 Ichinose H, University of Tokyo, private communication.

37 Kirkland A I, Saxton W O, Chau K-L, Tsuno K, and Kawasaki M (1995) Super-resolution by aperature synthesis: tilt series reconstruction in CTEM. *Ultramicroscopy* **57**: 355–374.

38 Chen W J and Chen F-R (1993) The atomic structure of $\Sigma = 1$ and $\Sigma = 3$ NiSi$_2$ / Si interface. *Philos. Mag.* **68A**: 605–630.

39 Buschmann V, Rodewald M, Fuess H, Van Tendeloo G, and Schaffer C (1999) High resolution electron microscopy study of molecular beam epitaxy grown CoSo$_2$/ Si$_{1-x}$Ge$_x$ / Si(100). *J. Appl. Phys.* **85**: 2119–2123.

40 Youssef S B, Fnaiech M, Chen F-R, Loubradou M, and Bonnet R (1999) Electron microscopy of nanoedges at the (001)InAs / (001)GaAs interface for an approximate orientation relationship. *Phys. Stat. Sol* (*a*) **174**: 403–411.